Toward a Better Understanding of Wildfire Behavior in the Wildland-Urban Interface: A Case Study of the 2021 Marshall Fire

Timothy W Juliano[1], Neil Lareau[2], Maria Frediani[3], Kasra Shamsaei[2], Masih Eghdami[1], Karen A Kosiba[4], Joshua Wurman[4], Amy DeCastro[5], Branko Kosović[1], and Hamed Ebrahimian[2]

[1]National Center for Atmospheric Research
[2]University of Nevada, Reno
[3]NCAR
[4]University of Illinois at Urbana-Champaign
[5]Unknown

November 24, 2022

Abstract

On 30 December 2021, the Marshall Fire devastated the Boulder, Colorado region. The fire initiated in fine fuels in open space just southeast of Boulder and spread rapidly due to the strong, downslope winds that penetrated into the Boulder Foothills. Despite the increasing occurrence of wildland-urban interface (WUI) disasters, many questions remain about how fires progress through vegetation and the built environment. To help answer these questions for the Marshall Fire, we use a coupled fire-atmosphere model and Doppler on Wheels (DOW) observations to study the fire's progression as well as examine the physical drivers of its spread. Evaluation of the model using the DOW suggests that the model is able to capture general characteristics of the flow field; however, it does not produce as robust of a hydraulic jump as the one observed. Our results highlight limitations of the model that should be addressed for successful WUI simulations.

Toward a Better Understanding of Wildfire Behavior in the Wildland-Urban Interface: A Case Study of the 2021 Marshall Fire

Timothy W. Juliano[1], Neil Lareau[2], Maria E. Frediani[1], Kasra Shamsaei[2], Masih Eghdami[1], Karen Kosiba[3], Joshua Wurman[3], Amy DeCastro[1], Branko Kosović[1], Hamed Ebrahimian[2]

[1]Research Applications Laboratory, National Center for Atmospheric Research
[2]University of Nevada, Reno
[3]University of Illinois at Urbana–Champaign, Champaign, Illinois

Key Points:

- Complex meso- and micro-scale meteorology, along with fire ember spotting, were responsible for rapid spread of the Marshall Fire
- Radar observations from "Doppler on Wheels" elucidates three-dimensional flow structures that impact fire and plume evolution
- Initial fire propagation in dry, fine fuels is well-represented by the coupled WRF-Fire model, but urban spread remains a challenge

Corresponding author: Timothy W. Juliano, `tjuliano@ucar.edu`

Abstract

On 30 December 2021, the Marshall Fire devastated the Boulder, Colorado region. The fire initiated in fine fuels in open space just southeast of Boulder and spread rapidly due to the strong, downslope winds that penetrated into the Boulder Foothills. Despite the increasing occurrence of wildland-urban interface (WUI) disasters, many questions remain about how fires progress through vegetation and the built environment. To help answer these questions for the Marshall Fire, we use a coupled fire-atmosphere model and Doppler on Wheels (DOW) observations to study the fire's progression as well as examine the physical drivers of its spread. Evaluation of the model using the DOW suggests that the model is able to capture general characteristics of the flow field; however, it does not produce as robust of a hydraulic jump as the one observed. Our results highlight limitations of the model that should be addressed for successful WUI simulations.

Plain Language Summary

Wildland-urban interface, or WUI, fires are increasing in the United States and around the world as the built environment continues to expand into the wildland. To better inform real-time management of active wildfires, it is critical that the scientific community can better predict WUI fire spread. In this study, we rely on multiple observational platforms, including the "Doppler on Wheels" radar, to investigate the performance of a state-of-the-art, coupled fire-atmosphere model during the Marshall Fire, which was a recent WUI fire that occurred in Colorado. While the modeling system performs well during the fire's initial propagation in fine fuels, it is unable to accurately predict spread in the built environment. While mesoscale to microscale simulations can accurately represent atmospheric flow features, more reliable predictability of wildfire behavior in the WUI will require consideration of urban fuels and fire ember spotting.

1 Introduction

Wildfire activity in the United States (U.S.) and across the globe has increased markedly over the last several decades (e.g., Westerling et al., 2006; Dennison et al., 2014; Balch et al., 2017; Iglesias et al., 2022). In the U.S., many of the recent wildfire seasons have involved long and intense burning periods, leading to the loss of life and property, as well as poor air quality (e.g., Buchholz et al., 2022) and reductions in solar energy production as a result of smoke generation (e.g., T. W. Juliano et al., 2022). Global climate models suggest that the recent trend of more large-scale fire events will continue and even increase in the future (e.g., Yue et al., 2013; Yoon et al., 2015; Abatzoglou & Williams, 2016). As part of the complexity, the so-called wildland-urban interface (WUI) is rapidly growing (e.g., Radeloff et al., 2018; Burke et al., 2021) and, therefore, amplifying the direct threat of wildfires on daily human activities.

Several notable WUI fires have occurred over the past decade in the U.S., primarily in California, including the Tubbs Fire (2017; e.g., Coen et al., 2018; Mass & Ovens, 2019), Camp Fire (2018; e.g., Brewer & Clements, 2019; Mass & Ovens, 2021), Woolsey Fire (2018; e.g., Keeley & Syphard, 2019), and Thomas Fire (2017; e.g., Fovell & Gallagher, 2018). One commonality between these wildfires is that they were considered wind-driven fires, allowing them to expand rapidly and wreak havoc on communities in their paths. In California, so-called "Santa Ana" (e.g., Randles et al., 2003, and references therein) or "Diablo" (e.g., Liu et al., 2021) wind events are often associated with destructive wind-driven wildfires (e.g., Nauslar et al., 2018; Smith et al., 2018). Wind-driven WUI fires are also a concern in regions outside of the U.S., including Australia (e.g., Cruz et al., 2012), France (e.g., Ganteaume, 2020), and Greece (e.g., Efthimiou et al., 2020).

The Marshall Fire is an example of a catastrophic wind-driven, WUI fire event that occurred just outside of Boulder, Colorado, U.S. on 30 December 2021 (Fovell et al., 2022), causing two deaths and destroying more than 1,000 buildings, leading to over $500 M in damages. The fire ignited near the Marshall Mesa during strong wind conditions (wind gusts over 40 m s^{-1}), and it began spreading rapidly in dry, fine fuels driven by intense, westerly winds. Approximately one hours after ignition, the fire transitioned into an urban conflagration, including "hopping" a six-lane interstate, Highway-36, via ember spotting. The large-scale meteorological setup favored a downslope windstorm along the Front Range (Fovell et al., 2022), which is a relatively common occurrence in this geographical region during the cold season (e.g., Whiteman & Whiteman, 1974; Durran, 1990).

In this study, we use observations and numerical simulations to examine the impact of the meso- and micro-scale meteorology on the Marshall Fire behavior. Specifically, we use a state-of-the-art numerical framework, the Weather Research and Forecasting (WRF) model with a fire behavior model (WRF-Fire), as well as measurements from the Doppler on Wheels (DOW) radar system, to address the following fundamental questions related to the topic of wildfire-weather: (1) *What were the observed and modeled atmospheric flow characteristics during the Marshall Fire?* and (2) *How well does the WRF-Fire model reproduce the Marshall Fire spread in the WUI?*

2 Data and Methods

2.1 WRF-Fire Model

The WRF model is a numerical weather prediction system used widely by research and operational forecasting communities alike (Skamarock et al., 2019). WRF has proven to be a powerful tool for simulating the full range of atmospheric scales, including meso- and micro-scales (e.g., Mazzaro et al., 2017; Muñoz-Esparza et al., 2017; Rai et al., 2019). Here, we utilize WRF in a one-way nested, mesoscale to microscale configuration (e.g., Haupt et al., 2019) whereby the inner domain is turbulence-resolving. The WRF domains are positioned to capture the westerly inflow that plays an important role on the wildfire propagation (Fig. S1). Our model setup and physics options closely follow those used in a recent study of the East Troublesome Fire by our team (DeCastro et al., 2022), and additional details may be found in Text S1.

To examine the Marshall Fire evolution, we conduct WRF simulations with a fire behavior model based on the Coupled Atmosphere-Wildland Fire Environment (Clark et al., 2004; Coen, 2013). This coupled fire-weather model is called WRF-Fire (Coen et al., 2013; Shamsaei et al., 2022). In addition to the meteorological grid that is defined in a standard WRF simulation, a fire grid is also required for a WRF-Fire simulation. The fire grid is refined by a factor of four relative to the meteorological grid (Δx = Δy = 27.78 m) to track the evolution of the fire perimeter via an improved level-set method (Muñoz Esparza et al., 2018) and compute small-scale changes in the fuel properties. The fire mesh is assigned fuel properties according to the Anderson 13 class fuel model (Anderson, 1981, Fig. S2) and topography according to 3-arc second Shuttle Radar Topography Mission terrain data. Using the parameterization developed by Rothermel (1972), the near-surface atmospheric winds, fuel characteristics, and terrain slope dictate the fire rate of spread. After a fire is ignited in the model, the fuel burn rate is calculated according to Albini and Reinhardt (1995). The amount of heat and moisture released back into the atmosphere is computed as a function of fuel properties, allowing for full coupling between the fire and atmosphere. Text S2 provides discussion on the model ignition times and locations, including the importance of ember spotting.

2.2 DOW Measurements

The DOW platform was deployed during the Marshall Fire to capture the three-dimensional smoke/ash plume and flow structures. Operating at 3-cm wavelength, the DOW is a mobile/quick deployable Doppler radar with high spatial resolution (50 x 160 $\times$ 160 m at 10 km range), allowing it to measure microscale structures (Wurman et al., 1997, 2021). During this deployment, the DOW operated mostly in a rastered Plan Position Indicator (PPI) scanning mode, with elevation scans ranging from $\sim$ 0.5 - 23 degrees (adjusted throughout the deployment) above the horizon. Parameters derived from the DOW observations and relevant to this study include reflectivity, radial velocity, and spectrum width. Reflectivity scans from the DOW provide information about the number and size of scatterers [fire-generated debris, or pyrometeors (McCarthy et al., 2019)] present in a retrieval volume, and, therefore, they may be used as a proxy for understanding the intensity of combustion and relative concentration of pyrometeors. The radial velocity product reveals flow moving away and toward the radar location (along the radar beam's path), while the spectrum width field indicates the variability of scatterer velocities in the retrieval volume and, therefore, it may be used as a proxy for turbulence levels.

3 Fire Spread in the WUI

The Marshall Fire had two reported initial ignition points, occurring at 18:08 and 19:00 UTC and approximately several 100s of meters apart (see Text S2 for more information). Thus, in our WRF-Fire simulations, we first ignite two separate fires. Both ignition points were in dry, short grass fuels. During the early stages of the fire, the combination of fuels and strong ($\sim$25 m s^{-1}), westerly winds supported rapid fire growth in the Marshall Mesa area (magenta star in Fig. 1). At 19:00 UTC, the initial burn region in the model takes on a finger-like structure, with spotting on the east and southern flanks as it approaches Highway 36 (Fig. 1).

According to Visible Infrared Imaging Radiometer Suite (VIIRS) fire detections at 19:25 UTC, the fire had spotted across Highway-36 to cause secondary ignitions (Fig. S3), but the simulated fire does not cross the highway via spotting until 19:45 UTC (cf. Fig. 1), at which time another burning lobe to the south originating from the second ignition has nearly reached the interstate. Two snapshots from VIIRS shortly after, at 20:15 UTC and 21:00 UTC (Fig. S3), show that the modeled leading edge is too slow and the north-south expansion is too narrow. We note that during this $\sim$1.5 h period, the intense westerly winds continue across much the region; however, the model shows weaker westerlies and even "reversed" flow intruding (further discussed in Section 4).

By mid-afternoon (22:05 UTC), the rapid fire spread is halted in the model as it reaches the urban region (Fig. 1), where non-burnable fuels are present in the model fuel layer. The westerly, low-level flow is confined to only the western potion of the area, with winds near the fire front opposing the original fire spread direction. This flow transition will be discussed further in Section 5. Nonetheless, around this time, the DOW reflectivity isosurfaces show active plume cores in two of the main fingers further north and east (Fig. 2a), confirming that the model is not able to capture the rapid and consequential propagation across the Highway-36.

Between 22:05 and 23:00 UTC, the model shows generally slower fire spread compared to previous hours, as it expands the burned region mostly to the north and south due to the relatively weak, variable winds (Fig. 1). During this time, and over the next couple of hours, the radar reflectivity isosurfaces indicate that the fire becomes increasingly active in the middle finger (Fig. 2b,c) before dissipating, while a new southern finger becomes more active (Fig. 2d). Only by the evening (02:30 UTC) does the simulated burn area finally spread into Louisville on the north side of Highway-36 and toward the southernmost observed finger (Fig. 1). In Section 5, we will discuss potential sources of error in the WRF-Fire simulations.

4 Horizontally Heterogeneous Wind Field

The synoptic-scale and mesoscale meteorology during the Marshall Fire event fostered intense downslope winds along the Front Range (Fovell et al., 2022). A north-south band of strong, westerly flow (gusts >30 m s^{-1}) was positioned along the Boulder Foothills, where the plunging, downslope flow remained attached at the surface, including in the vicinity of the Marshall Fire ignitions. In contrast, many locations not too far to the east generally experienced weaker winds (gusts <20 m s^{-1}) where the flow detached from the surface, as shown in Fig. 1 and in agreement with Fovell et al. (2022, their Fig. 1). To evaluate the WRF-Fire model's ability to represent the spatially variable, low-level flow during the event, in Fig. S4 we compare observed and modeled time series of the surface stations shown in Fig. S1 and described in Text S3. By and large, the model performs better at the western stations, where strong, westerly winds persisted before the flow transitioned. Even still, WRF tends to underestimate the strongest wind gusts of 40-50 m s^{-1} that were observed at CO1 and BLD. This result supports the aforementioned underestimation in model fire spread. Compared to the western area, both observations and WRF show much more variable wind speeds and directions toward the east of the fire.

The horizontal structure and variability in the wind field is captured by the DOW radial velocity observations. Figure 3a shows the time-mean radial velocity for scans below 5 degrees, revealing (*i*) the strong west-southwest winds across the fire, (*ii*) a region of reversed flow, especially over the southern portions of the fire area, and (*iii*) a subsequent return to west winds aloft and to the east. In Fig. 3b, we also show the fraction of the time the radial wind is positive. These data show that within the time-mean reversed flow regions, many locations experience positive winds ∼50% of the time, suggesting that the winds were substantially variable. As we will discuss in the next section, the flow variability is related to the presence of a hydraulic jump. Shown in both plots are also station observations (colored circles) that indicate the radial wind component and the vector wind during the averaging period (Fig. 3a), as well as the fraction of time with positive winds at each site (Fig. 3b). Overall, the agreement between the radar and near-surface observations is good; however, some differences are expected because the height of the radar retrieval volume increases as the radial distance increases according to the DOW scan angle (not shown).

5 Vertical Structure and Flow Evolution

Based on quasi-idealized simulations, Fovell et al. (2022) suggest that a "hydraulic jump-like feature" was present downwind of the strongest winds in the Boulder Foothills. To further explore this aspect of the atmospheric flow, we use model output and DOW observations. In Fig. 4, we present east-west vertical cross-sections of the zonal wind component. Each panel represents a different snapshot in time, with the times corresponding to those shown in Fig. 1. Throughout the event, the low-level, downslope winds upstream of the fire (west of ∼105.3°W) are consistently strong and capped by a strong inversion where winds diminish quickly with height. This band of intense winds continues eastward, bringing strong westerlies into the Boulder Foothills during the early stages of the Marshall Fire, and rising with height toward the east (Fig. 4). As a result, the atmospheric flow supports the fire's rapid advancement around 1900 UTC (cf. Fig. 1). Over the ensuing hours, the wind maxima retreats westward, and eventually the well-defined vertical structure breaks down into a more chaotic structure further east (Fig. 4). The strong inversion erodes where the intense winds diminish, as the wavy isentropes (solid green lines) suggest strong vertical mixing within the lower-levels. In the transition zone, a hydraulic jump is evident with a sharp decrease, and even complete reversal, in the zonal winds and vertical displacement of the isentropes.

The transition from strong flow in a shallow boundary layer to weaker winds as the boundary layer deepens further downwind, with turbulence production in between, are classical characteristics of a hydraulic jump (e.g., Ball, 1956; T. W. Juliano et al., 2017). To probe the dynamical support for the presence of a hydraulic jump, we conduct a Froude Number (Fr) analysis along the vertical cross-sections shown in Fig. 4. Results presented in Fig. S5 indicate a transition from supercritical (Fr >1) to subcritical flow (Fr <1) – a well-known requirement for the presence of a hydraulic jump. Upstream Fr values between 2 and 4 (Fig. S5 and Text S4) suggest a hydraulic jump with a roller (e.g., Chanson, 2009), whereby much of the mean kinetic energy is converted into turbulent kinetic energy (TKE). In this particular case, the WRF model simulates an extraordinary transition, with maximum TKE values exceeding 200 m^2 s^{-2} due to the strong decay in intense westerly winds (Fig. S6).

The hydraulic jump and subsequent gravity wave structures in Fig. 4 are readily apparent in a cross section of the radar reflectivity spanning 2202-2226 UTC (Fig. 5). Specifically, the DOW data show a leading wave linked to the fire's updraft that is embedded in the hydraulic jump region followed by a subsidence region (i.e., diminishing plume heights) and a second wave crest (Fig. 5a). Spectrum width measurements (Fig. S7) show maximum values in the primary plume with a secondary maximum in the downstream wave (qualitatively similar to the TKE field from WRF; cf. Fig. S6). The contemporaneous isentropes extracted from WRF suggest that the simulation underestimates the injection height of smoke and ash in the leading wave. This discrepancy may be due to a lack of urban fuels in the model: the combustion of urban fuels, which have high fuel loads and long residence times, may have produced more intense heat release in reality compared to what was simulated. Nonetheless, the structure of the second wave agrees fairly well between observations and simulations. Also shown is the downwind variation of the column maximum radar reflectivity (Fig. 5b), which is a measure of plume dilution and debris fall out. The maximum reflectivity (uncorrected) is ∼30 dbZ, with a logarithmic decay to the east. The sharpest reduction in reflectivity is close to the main updraft, suggesting the potential for ember fall out in this region.

6 Discussion and Conclusions

In this article, we present observations and numerical model simulations of the Marshall Fire in December 2021, which spread rapidly in the WUI due to strong, westerly winds along with dry, fine fuels and ember spotting. Observations from surface stations near the fire show that the WRF-Fire model generally underestimates the strongest recorded wind speeds, leading to a slightly slower propagation through the wildland fuels west of Highway-36. Satellite measurements at the beginning of the event confirm the model's slower spread prior to the fire reaching the towns of Superior and Louisville.

We also rely on data from the DOW radar – deployed several hours after the initial ignition – to highlight the three-dimensional atmospheric flow structure during the wildfire. The radar retrievals illustrate substantial horizontal variability in the low-level wind field, in addition to vertical plume structure embedded in a robust hydraulic jump. Turbulence-resolving output from WRF-Fire suggests that the highly variable, low-level winds are related to the hydraulic jump. In this jump region, the flow transitions from intense westerlies to much weaker westerlies or even a shift to easterlies, ultimately affecting the Marshall Fire spread rate and direction.

Even though the model produces generally encouraging results, there are two main shortcomings related to the fire module in WRF that should be discussed. First, while the most up-to-date version of WRF-Fire as of this writing (version 4.4) contains a firebrand parameterization, it does not ignite spot fires, but rather provides only a likelihood of spot fire ignition. Rapid wildfire spread is often caused by embers generating new ignitions ahead of the main fire front (e.g., N. P. Lareau et al., 2022). The Marshall

Fire was able to cross Highway-36, which is a six-lane interstate. Such advancement is possible only through ember spotting, and, therefore, a WRF-Fire simulation – without additional manual ignitions such as in this study – is not able to produce further fire spread.

Second, the WRF-Fire model must be improved to account for WUI fuels and related fire propagation in the built environment. During post-fire investigations of the Marshall Fire, the Institute for Business and Homes Safety found evidence that wooden fences falling between homes in Superior and Louisville were a primary cause of fire spread (Reppenhagen, 2022). At present, the WRF-Fire model contains fuel categories (based on Anderson 13) strictly intended for fires in the wildland and a rate of spread parameterization (based on Rothermel) developed without considering fire-atmosphere coupling. However, given the increasing trend in WUI fire occurrence, fuel maps including WUI materials, as well as improved representation of fire spread, should be developed for coupled fire-atmosphere models. The WUI challenge highlights the urgent need to better understand the complex interactions between humans and the built environment, weather, and wildfire, and ultimately develop more effective solutions to predict wildfire behavior and risk.

7 Open Research

7.1 Data Availability Statement

Surface weather station data and model outputs (`https://doi.org/10.7910/DVN/M6WCBT`; T. Juliano et al., 2022), as well as VIIRS fire detections (`https://doi.org/10.7910/DVN/PR6XDM`; T. Juliano & Shamsaei, 2022), used in this study are stored on Harvard Dataverse and will be finalized prior to publication. DOW measurements are available at (`https://doi.org/10.48514/JKJ0-TE44`; Wurman & Kosiba, 2022). Users should contact Josh Wurman (jwurman@illinois.edu) or Karen Kosiba (kakosiba@illinois.edu) to gain access to the data.

7.2 Software Availability Statement

The WRF v4.4 code used for the simulations is publicly available on Github (`https://github.com/wrf-model/WRF/tree/release-v4.4`). Codes for the model (`https://doi.org/10.7910/DVN/M6WCBT`; T. Juliano et al., 2022) and DOW (`https://doi.org/10.7910/DVN/KYSLUE`; N. Lareau, 2022) analyses are available on Harvard Dataverse and will be finalized prior to publication.

Acknowledgments

The National Center for Atmospheric Research (NCAR) is a major facility sponsored by the National Science Foundation (NSF) under Cooperative Agreement No. 1852977. The authors are grateful for funding provided by NSF (Award #1953333). We would like to acknowledge the use of computational resources (doi:10.5065/D6RX99HX) at the NCAR-Wyoming Supercomputing Center provided by the NSF and the State of Wyoming, and supported by NCAR's Computational and Information Systems Laboratory.

References

Abatzoglou, J. T., & Williams, A. P. (2016). Impact of anthropogenic climate change on wildfire across western US forests. Proc. Natl. Acad. Sci. USA, *113*, 11770-11775.

Albini, F. A., & Reinhardt, E. D. (1995). Modeling ignition and burning rate of large woody natural fuels. Int. J. Wildland Fire, *5*(2), 81-91.

Anderson, H. E. (1981). *Aids to determining fuel models for estimating fire behavior* (Vol. 122). US Department of Agriculture, Forest Service, Intermountain Forest and Range Experiment Station.

Balch, J. K., Bradley, B. A., Abatzoglou, J. T., Nagy, R. C., Fusco, E. J., & Mahood, A. L. (2017). Human expansion of the fire niche. Proc. Natl. Acad. Sci. USA, *114*, 2946-2951.

Ball, F. K. (1956). The theory of strong katabatic winds. , *9*, 373-386.

Brewer, M. J., & Clements, C. B. (2019). The 2018 Camp Fire: Meteorological analysis using in situ observations and numerical simulations. Atmosphere, *11*(1).

Buchholz, R. R., Park, M., Worden, H. M., Tang, W., Edwards, D. P., Gaubert, B., ... Magzamen, S. (2022). New seasonal pattern of pollution emerges from changing North American wildfires. Nat. Commun., *13*.

Burke, M., Driscoll, A., Heft-Neal, S., Xue, J., Burney, J., & Wara, M. (2021). The changing risk and burden of wildfire in the United States. Proc. Natl. Acad. Sci. USA, *118*(e2011048118).

Chanson, H. (2009). Current knowledge in hydraulic jumps and related phenomena: A survey of experimental results. European Journal of Mechanics B/Fluids, *28*, 191-210.

Clark, T. L., Coen, J., & Latham, D. (2004). Description of a coupled atmosphere–fire model. J. Wildland Fire, *13*, 49-63.

Coen, J. L. (2013). A description of the Coupled Atmosphere-Wildland Fire Environment model (CAWFE). *National Center for Atmospheric Research: Boulder, CO, USA*, *38*.

Coen, J. L., Cameron, M., Michalakes, J., E. G. Patton, E., Riggan, P. J., & Yedinak, K. M. (2013). WRF-Fire: Coupled weather–wildland fire modeling with the Weather Research and Forecasting model. J. Appl. Meteor. Clim., *52*, 16-38.

Coen, J. L., Schroeder, W., & Quayle, B. (2018). The generation and forecast of extreme winds during the origin and progression of the 2017 Tubbs Fire. Atmosphere, *9*(12).

Cruz, M. G., Sullivan, A. L., Gould, J. S., Sims, N. C., Bannister, A. J., Hollis, J. J., & Hurley, R. J. (2012). Anatomy of a catastrophic wildfire: the Black Saturday Kilmore East Fire in Victoria, Australia. Forest Ecology and Management, *284*, 269-285.

DeCastro, A. L., Juliano, T. W., Kosović, B., Ebrahimian, H., & Balch, J. K. (2022). A computationally efficient method for updating fuel inputs for wildfire behavior models using Sentinel imagery and random forest classification. Remote Sens., *14*(6).

Dennison, P., Brewer, S., Arnold, J., & Moritz, M. (2014). Large wildfire trends in the western United States. Geophys. Res. Let., *41*, 2928-2933.

Durran, D. R. (1990). Mountain waves and downslope winds. In W. Blumen (Ed.), *Atmospheric processes over complex terrain, Meteorological Monographs* (Vol. 23, p. 59-81). American Meteorological Society.

Efthimiou, N., Psomiadis, E., & Panagos, P. (2020). Fire severity and soil erosion susceptibility mapping using multi-temporal Earth Observation data: The case of Mati fatal wildfire in Eastern Attica. Catena, *187*(104320).

Fovell, R. G., Brewer, M. J., & Garmong, R. J. (2022). The December 2021 Marshall Fire: Predictability and gust forecasts from operational models. Atmosphere, *13*(5).

Fovell, R. G., & Gallagher, A. (2018). Winds and gusts during the Thomas Fire. Fire, *1*(3).

Ganteaume, A. (2020). Role of ornamental vegetation in the propagation of the Rognac Fire. In S. M. Hood, S. Drury, T. Steelman, & R. Steffens (Eds.), *Proceedings of the fire continuum-preparing for the future of wildland fire* (p. 25-64). Fort Collins, CO: US Department of Agriculture, Forest Service, Rocky Mountain Research Station: A Special Report of Working Groups I and II of the Intergovernmental Panel on Climate Change (IPCC). Cambridge University Press.

Haupt, S. E., Kosović, B., Shaw, W., Berg, L. K., Churchfield, M., Cline, J., ... Sever, G. (2019). On bridging a modeling scale gap: Mesoscale to microscale coupling for wind energy. Bull. Amer. Meteor. Soc., *1009*(12), 2533-2550.

Iglesias, V., Balch, J., & Travis, W. R. (2022). U.S. fires became larger, more frequent, and more widespread in the 2000s. Science Advances, *8*.

Juliano, T., Frediani, M., Shamsaei, K., Eghdami, M., & Kosovic, B. (2022). *WRF-Fire files for "Toward a Better Understanding of Wildfire Behavior in the Wildland-Urban Interface: A Case Study of the 2021 Marshall Fire"*. Harvard Dataverse, V3. doi: https://doi.org/10.7910/DVN/M6WCBT

Juliano, T., & Shamsaei, K. (2022). *VIIRS files for "Toward a Better Understanding of Wildfire Behavior in the Wildland-Urban Interface: A Case Study of the 2021 Marshall Fire"*. Harvard Dataverse, V1. doi: https://doi.org/10.7910/DVN/PR6XDM

Juliano, T. W., Jiménez, P. A., Kosović, B., Eidhammer, T., Thompson, G., Berg, L. K., ... Polidori, A. (2022). Smoke from 2020 united states wildfires responsible for substantial solar energy forecast errors. Environ. Res. Lett., *17*(3).

Juliano, T. W., Parish, T. R., Rahn, D. A., & Leon, D. C. (2017). An atmospheric hydraulic jump in the Santa Barbara Channel. J. Appl. Meteor. Clim., *56*, 2981-2998.

Keeley, J. E., & Syphard, A. D. (2019). Twenty-first century California, USA, wildfires: fuel-dominated vs. wind-dominated fires. Fire Ecology, *15*(1).

Lareau, N. (2022). *DOW files for "Toward a Better Understanding of Wildfire Behavior in the Wildland-Urban Interface: A Case Study of the 2021 Marshall Fire"*. Harvard Dataverse, V1. doi: https://doi.org/10.7910/DVN/KYSLUE

Lareau, N. P., Donohoe, A., Roberts, M., & Ebrahimian, H. (2022). Tracking wildfires with weather radars. J. Geophys. Res. Atmos., *127*(e2021JD036158).

Liu, Y. C., Di, P., Chen, S. H., Chen, X., Fan, J., DaMassa, J., & Avise, J. (2021). Climatology of Diablo winds in northern California and their relationships with large-scale climate variabilities. Climate Dynamics, *56*, 1335-1356.

Mass, C. F., & Ovens, D. (2019). The Northern California wildfires of 8-9 october 2017: The role of a major downslope wind event. Bull. Amer. Meteor. Soc., *100*, 235-256.

Mass, C. F., & Ovens, D. (2021). The synoptic and mesoscale evolution accompanying the 2018 Camp Fire of Northern California. Bull. Amer. Meteor. Soc., *102*, E168-E192.

Mazzaro, L. J., Muñoz-Esparza, D., Lundquist, J. K., & Linn, R. R. (2017). Nested mesoscale-to-LES modeling of the atmospheric boundary layer in the presence of under-resolved convective structures. J. Adv. Model. Earth Syst., *9*, 1795–1810.

McCarthy, N., Guyot, A., Dowdy, A., & McGowan, H. (2019). Wildfire and weather radar: A review. J. Geophys. Res. Atmos., *124*, 266-286.

Muñoz-Esparza, D., Lundquist, J. K., Sauer, J. A., Kosović, B., & Linn, R. R. (2017). Coupled mesoscale-LES modeling of a diurnal cycle during the CWEX-13 field campaign: From weather to boundary-layer eddies. J. Adv. Model. Earth Syst., *9*, 1572–1594.

Muñoz Esparza, D., Kosović, B., Jiménez, P. A., & Coen, J. L. (2018). An accurate fire-spread algorithm in the Weather Research and Forecasting model using the level-set method. J. Adv. Model. Earth Syst., *10*, 908-926.

Nauslar, N. J., Abatzoglou, J. T., & Marsh, P. T. (2018). The 2017 North Bay and Southern California fires: a case study. Fire, *1*(18).

Radeloff, V. C., Helmers, D. P., Kramer, H. A., Mockrin, M. H., Alexandre, P. M., Bar-Massada, A., ... Stewart, S. I. (2018). Rapid growth of the US wildland-urban interface raises wildfire risk. Proc. Natl. Acad. Sci. USA, *115*, 3314-3319.

Rai, R. K., Berg, L. K., Kosović, B., Haupt, S. E., Mirocha, J. D., Ennis, B., &

Draxl, C. (2019). Evaluation of the impact of horizontal grid spacing in terra incognita on coupled mesoscale-microscale simulations using the WRF framework. Mon. Wea. Rev., *147*, 1007–1027.

Randles, C. A., da Silva, A. M., Buchard, V., Colarco, P. R., Darmenov, A., Govindaraju, R., ... Flynn, C. J. (2003). The Santa Ana winds of California. Earth Interactions, *7*(8).

Reppenhagen, C. (2022). Wood fences found to be pathways for marshall fire to spread between homes. *9NEWS*. Retrieved from `https://www.9news.com/article/news/local/wildfire/marshall-fire/wood-fences-pathways-for-marshall-fire-spread/73-7ba1eafc-196a-48c9-abfe-46f87189b2b4`

Rothermel, R. C. (1972). A mathematical model for predicting fire spread in wildland fuels. *USDA Forest Service Research Paper INT-115*.

Shamsaei, K., Juliano, T. W., Igrashkina, N., Ebrahimian, H., Kosović, B., & Taciroglu, E. (2022). *WRF-Fire Wikipage.* doi: 10.5281/zenodo.6667633

Skamarock, W. C., Klemp, J. B., Dudhia, J., Gill, D. O., Liu, Z., Berner, J., ... Huang, X.-Y. (2019). A description of the Advanced Research WRF version 4. NCAR Tech. Note NCAR/TN-556+STR.

Smith, C., Hatchett, B. J., & Kaplan, M. (2018). A surface observation based climatology of diablo-like winds in california's wine country and western sierra nevada. Fire, *1*(25).

Westerling, A. L., Hidalgo, H. G., Cayan, D. R., & Swetnam, T. W. (2006). Warming and earlier spring increase western U.S. forest wildfire activity. Science, *313*, 940-943.

Whiteman, D. C., & Whiteman, J. G. (1974). An historical climatology of damaging downslope windstorms at Boulder, Colorado. *NOAA technical report ERL; 336; NOAA technical report ERL. 35 APCL.*

Wurman, J., & Kosiba, K. (2022). *Flexible Array of Radars and Mesonets Marshal Fire (2021) Data (Version 1) [Data set].* Flexible Array of Radars and Mesonets, University of Illinois. doi: https://doi.org/10.48514/JKJ0-TE44

Wurman, J., Kosiba, K., Pereira, B., Robinson, P., Frambach, A., Gilliland, A., ... Lutz, J. (2021). The FARM (Flexible Array of Radars and Mesonets). Bull. Amer. Meteor. Soc., *102*, E1499-E1525.

Wurman, J., Straka, J., Rasmussen, E., Randall, M., & Zahrai, A. (1997). Design and deployment of a portable, pencil-beam, pulsed, 3-cm Doppler radar. J. Atmos. Oceanic Technol., *14*, 1502-1512.

Yoon, J., Wang, S.-Y. S., Gillies, R. R., Hipps, L., Kravitz, B., & Rasch, P. J. (2015). Extreme fire season in California: A glimpse into the future? Bull. Amer. Meteor. Soc., *96*, S5-S9.

Yue, X., Mickley, L. J., Logan, J. A., & Kaplan, J. O. (2013). Ensemble projections of wildfire activity and carbonaceous aerosol concentrations over the western United States in the mid-21st century. Atmos. Environ., *77*, 767-780.

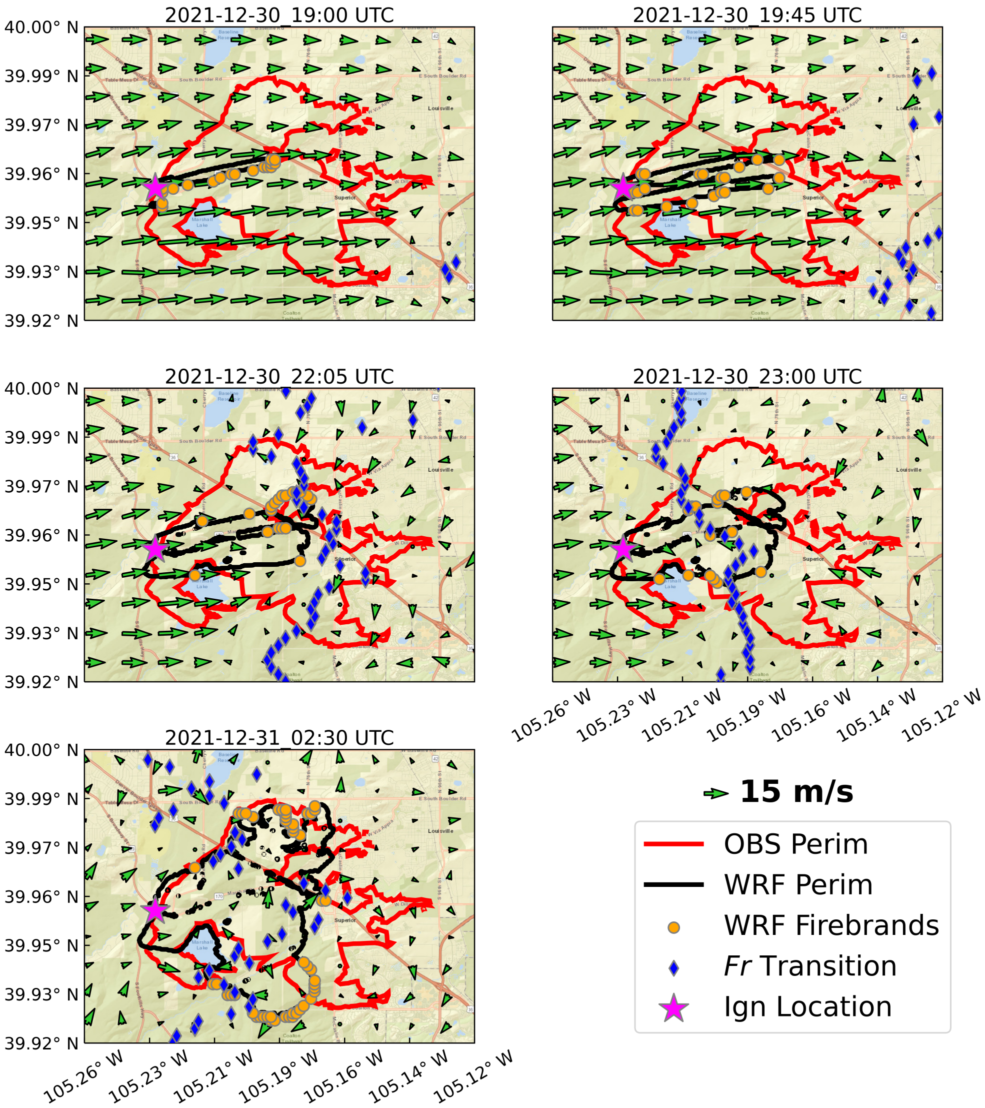

Figure 1. Temporal progression of the Marshall Fire spread. The magenta star represents the approximate location of the initial fire ignitions, while the red line represents the final observed perimeter and the black line represents the WRF-Fire perimeter at the indicated time. The orange circles represent firebrand landing locations according to WRF-Fire. Flow transitions from supercritical to subcritical are shown by the blue diamonds. Also shown are 10 m wind arrows according to the key.

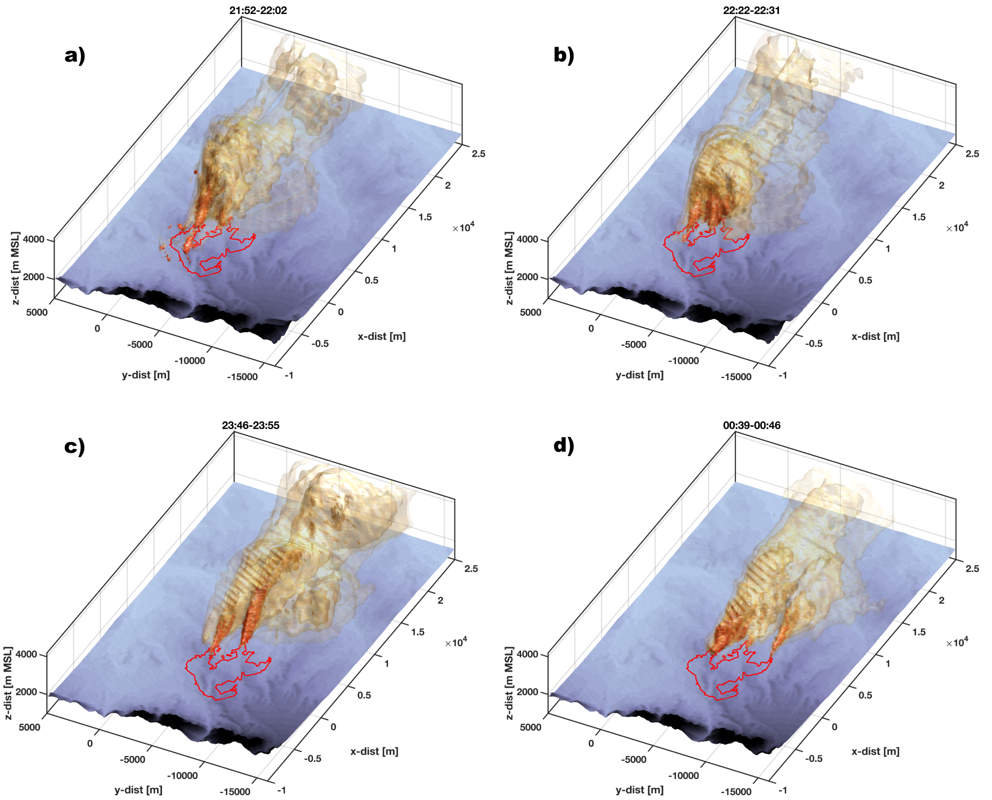

Figure 2. Radar reflectivity isosurfaces showing plume evolution. Transparent Isosurfaces are rendered at -10, 10, 15, 20, 23, 26, and 27 dbZ with colors becoming increasingly red for higher values. The data window (UTC), is shown at the top of each panel. Also shown are the IR fire perimeter (red contour) and terrain elevation (gray shaded relief).

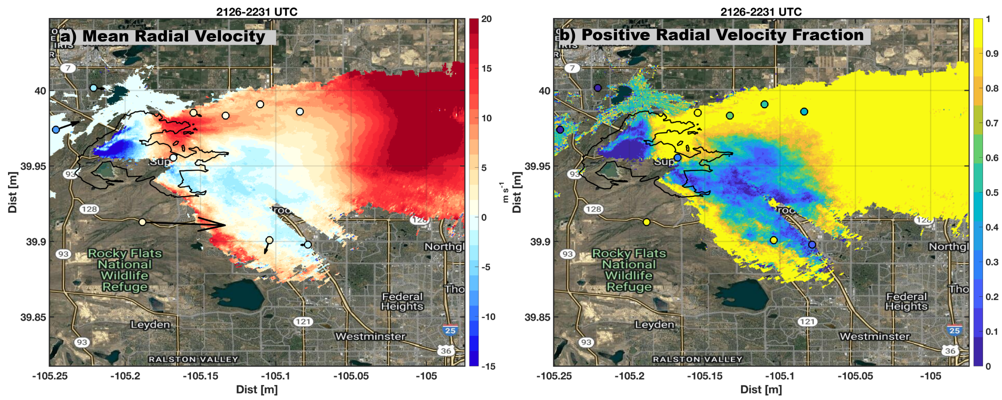

Figure 3. (a) Time-mean radial velocity data with station observations showing mean wind vectors and mean radial velocity (color shaded). (b) Fraction of the time with a positive radial wind component. Both figures also show the final observed perimeter (solid black contour).

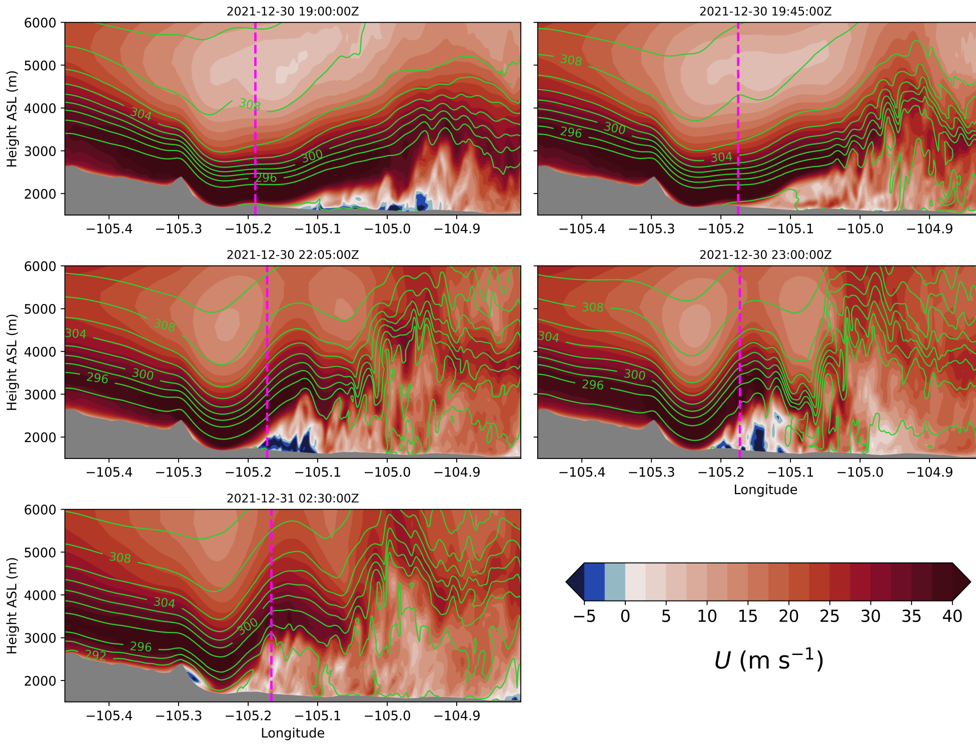

Figure 4. East-west vertical transects showing the U-component of the wind speed according to the colorbar, along with isentropes (potential temperature contours) every 2 K in green. The vertical magenta line represents the furthest eastward progression of the fire front in the whole domain. Gray shading represents the terrain profile. Times shown are the same as in Fig. 1.

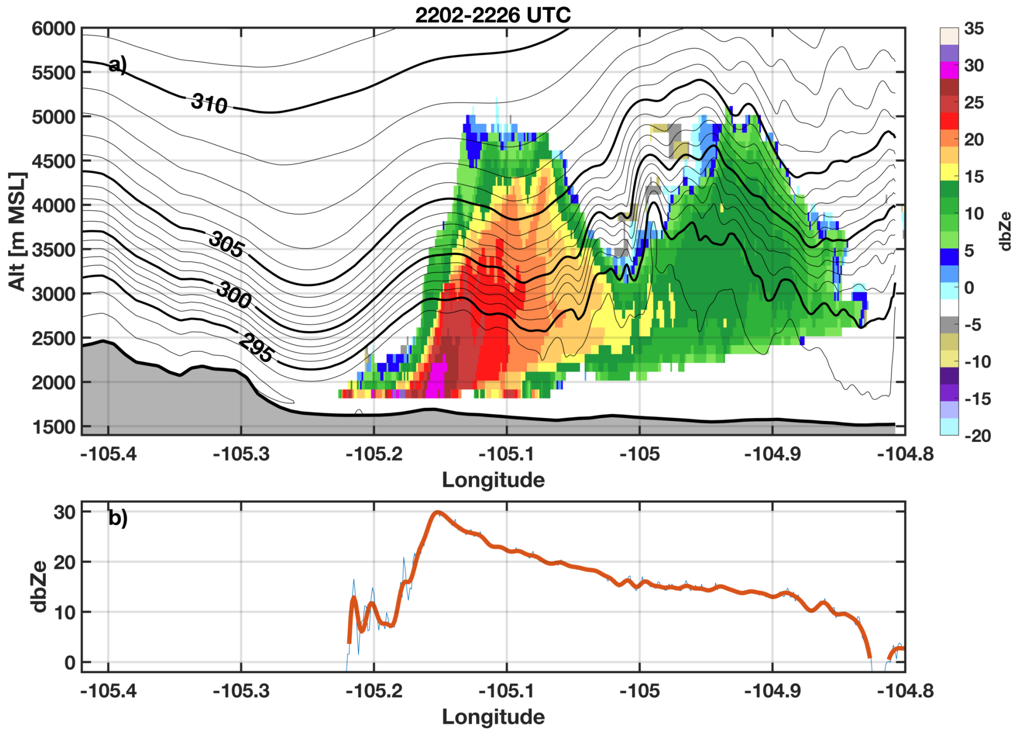

Figure 5. (a) Time and meridional maximum radar reflectivity cross section for the 2202-2226 UTC interval. Reflectivity values are shaded, with potential temperature contours from WRF (contours every 1 K, bold and labeled every 5 K). Gray shading represents the terrain profile. (b) Column maximum radar reflectivity as a function of longitude.

Supporting Information for "Toward a Better Understanding of Wildfire Behavior in the Wildland-Urban Interface: A Case Study of the 2021 Marshall Fire"

Timothy W. Juliano[1], Neil Lareau[2], Maria E. Frediani[1], Kasra Shamsaei[2], Masih Eghdami[1], Karen Kosiba[3], Joshua Wurman[3], Amy DeCastro[1], Branko Kosović[1], Hamed Ebrahimian[2]

[1]Research Applications Laboratory, National Center for Atmospheric Research

[2]University of Nevada, Reno

[3]University of Illinois at Urbana–Champaign, Champaign, Illinois

Contents of this file

1. Text S1-S4
2. Figures S1 to S7

S1: WRF model setup In our two domain configuration, the outer and inner domains are resolved using a horizontal grid cell spacing of $\Delta x = \Delta y = 1000$ m and 111.11 m, respectively. We use a total of 45 model grid cells in the vertical column and set the grid cell spacing, $\Delta z \approx 25$ m adjacent to the surface before stretching with increasing height. In the outer domain, we activate the Yonsei University (YSU) planetary boundary layer

(PBL) parameterization (Hong et al., 2006) to handle vertical turbulent mixing, and 2D horizontal diffusion is computed by Smagorinsky (1963). In the inner domain, we turn off the PBL scheme and use WRF's large-eddy simulation capability by activating the three-dimensional turbulent kinetic energy (TKE)-based sub-grid scale (SGS) model of Deardorff (1980). Details about the resolved TKE calculation is described in Text S4.

S2: Marshall Fire ignition approach The first ignition, initially reported by a 911 call at 18:08 UTC, was slightly northeast of the intersection of Marshall Road and Highway-93 (approximate location: 39.956127°N, 105.230487°W). The 911 call indicated that a structure was burning uncontrollably in the intense winds. At 19:00 UTC, a Boulder park ranger on the scene noticed a second ignition location to the southwest, near the Marshall Mesa Trailhead parking lot (approximate location: 39.951209°N, 105.231441°W). This ignition occurred in dry, fine fuels and began spreading rapidly toward the northeast. In the WRF-Fire simulations, we ignite these two sources according to the above information.

Other ignitions also occurred later during the Marshall Fire likely due to ember spotting. Without any conclusive information, we hypothesize that ember spotting is the only plausible way that the fire was able to "hop" across Highway-36. Therefore, we use the firebrand spotting parameterization (Frediani et al., 2021) in WRF-Fire to produce spotting likelihood maps. We first run a simulation with only the two aforementioned primary ignitions and allow the fire to approach Highway-36. At this stage, the fire is not able to propagate further because any roadways in the fuel model are considered non-burnable fuel. However, we use the spotting parameterization to estimate where and when new ignitions are most likely to occur. While this approach is somewhat subjective, we believe that it is reasonable, especially because the modeled fire spread appears realistic in the fine fuels. Technical details about the WRF-Fire spotting parameterization may be found in Appendix A of the WRF User Guide starting in v4.4 (`https://www2.mmm.ucar.edu/wrf/users/docs/user_guide_v4/v4.4/users_guide_chap-fire.html#firebrand`).

Two additional fire ignition locations and times, based on the spotting parameterization, are estimated: (39.9638°N, 105.180°W) at 19:40 UTC and (39.966248°N, 105.185050°W) at 20:30 UTC. We then conduct a second WRF-Fire simulation with these additional spotting ignitions and present the results in the main manuscript.

S3: Fr **calculation** The dimensionless Fr, which is often used to examine atmospheric flow adjustment, may be interpreted as the ratio of the mean planetary boundary layer (PBL) wind speed to the fastest possible gravity wave traveling along the fluid interface between the PBL and free troposphere. For the Fr analysis, we follow a similar approach as in (Juliano et al., 2017). Here the PBL height is determined based on the sharpest vertical gradient in the potential temperature field. Reduced gravity is computed as $g' = g\frac{\theta_t - \overline{\theta_{PBL}}}{\overline{\theta_{PBL}}}$ where θ_t is the free troposphere potential temperature, $\overline{\theta_{PBL}}$ is the mean PBL potential temperature (and so $\theta_t - \overline{\theta_{PBL}}$ represents the change in θ across the PBL inversion). For θ_t, we use the θ value from two grid cells above the defined PBL top. The Fr is then calculated as $Fr = \frac{V}{\sqrt{g'H}}$ where H is the PBL depth and V is the mean PBL wind speed.

S4: TKE calculation In this study, we use the TKE field to better understand the presence of a hydraulic jump (i.e., supercritical to subcritical flow transition). To compute the resolved TKE from the WRF output, we follow steps outlined in previous studies (e.g., Schmidli, 2013; Wagner et al., 2014). First, we decompose a fully turbulent variable, ϕ, into its model grid cell average (represented by the instantaneous model output), $\overline{\phi}$, and unresolved, $\phi^{'}$, components:

$$\phi(x,y,z,t) = \overline{\phi}(x,y,z,t) + \phi^{'}(x,y,z,t)$$

where (x, y, z, t) represents the space and time dimensions. The unresolved component is computed by the large-eddy simulation SGS model and output at each (x, y, z) grid cell and time stamp (1 min sampling interval). The resolved turbulent component, $\phi^{''}$, is then calculated as

$$\phi^{''}(x,y,z,t) = \overline{\phi}(x,y,z,t) - \langle \overline{\phi}(x,y,z,t) \rangle$$

where $\langle\ \rangle$ represents a temporal average defined as

$$\langle\ \rangle = \frac{1}{T} \int_{t-T/2}^{t+T/2} \overline{\phi}(x,y,z,t)\, dt$$

with T representing the time-averaging interval. We choose $T = 40$ min with a 1 min sampling interval, which is similar to other studies (e.g., Juliano et al., 2017, 2022). Results are relatively insensitive when using $T = 20$ min with a 1 min sampling interval (not shown).

References

Deardorff, J. W. (1980). Stratocumulus-capped mixed layers derived from a three-dimensional model. Bound.-Layer Meteor., *18*, 495–527.

Frediani, M., Juliano, T. W., DeCastro, A., Kosović, B., & Knievel, J. (2021). A fire-spotting parameterization coupled with the wrf-fire model. *Earth and Space Science Open Archive*, 12. doi: 10.1002/essoar.10506771.1

Hong, S.-Y., Noh, Y., & Dudhia, J. (2006). A new vertical diffusion package with an explicit treatment of entrainment processes. Mon. Wea. Rev., *134*, 2318-2341.

Juliano, T. W., Kosović, B., Jiménez, P. A., Eghdami, M., Haupt, S. E., & Martilli, A. (2022). "Gray Zone" simulations using a three-dimensional planetary boundary layer parameterization in the Weather Research and Forecasting model. Mon. Wea. Rev., *150*, 1585-1619.

Juliano, T. W., Parish, T. R., Rahn, D. A., & Leon, D. C. (2017). An atmospheric hydraulic jump in the Santa Barbara Channel. J. Appl. Meteor. Clim., *56*, 2981-2998.

Schmidli, J. (2013). Daytime heat transfer processes over mountainous terrain. J. Atmos. Sci., *70*, 4041–4066.

Smagorinsky, J. (1963). General circulation experiments with the primitive equations: I. The basic experiment. Mon. Wea. Rev., *91*, 99–164.

Wagner, J. S., Gohm, A., & Rotach, M. W. (2014). The impact of horizontal model grid resolution on the boundary layer structure over an idealized valley. Mon. Wea. Rev., *142*, 3446–3465.

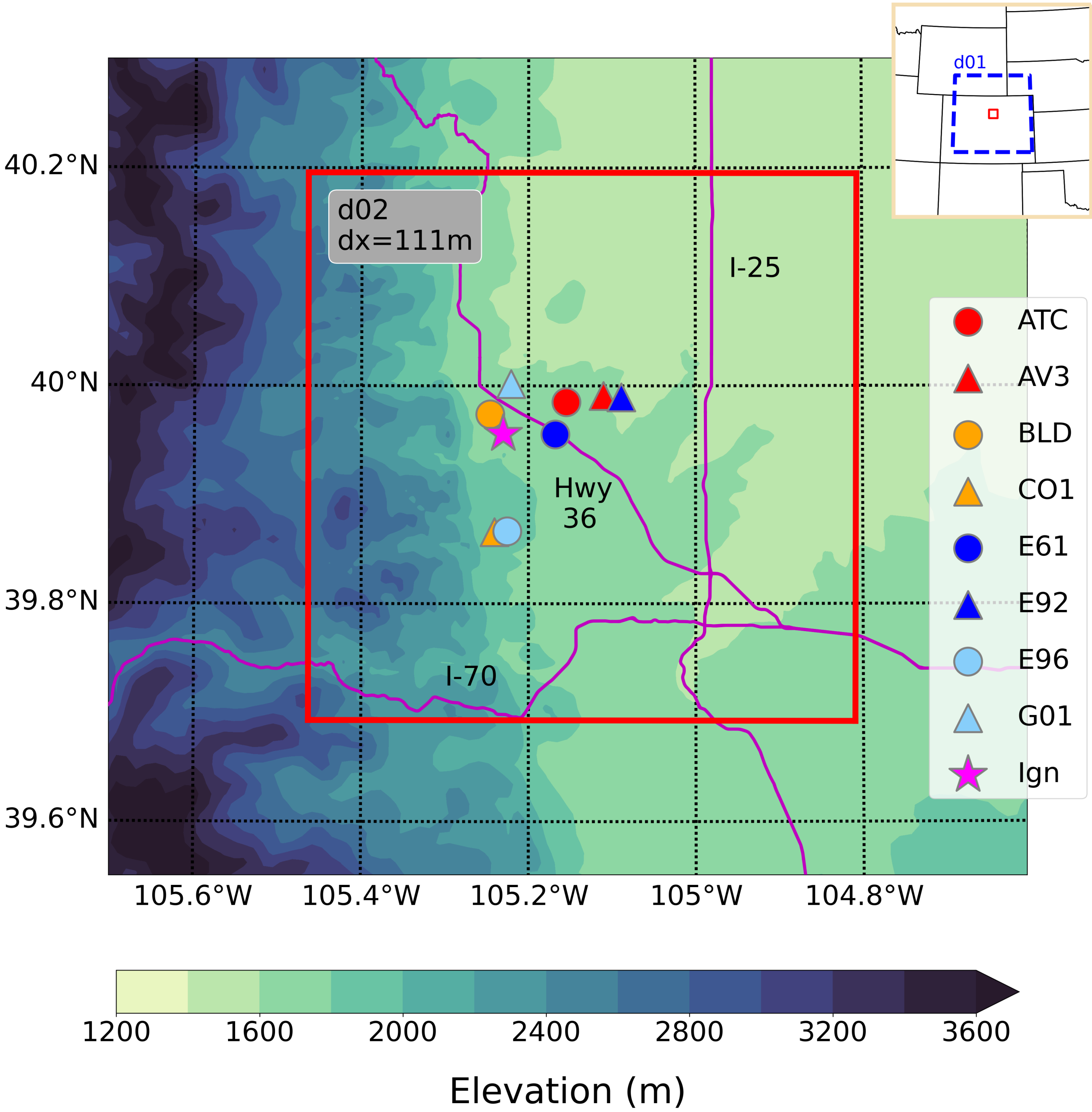

Figure S1. WRF-Fire domain configuration. The outer and inner domains are abbreviated as d01 and d02, respectively. The colored red, orange, and blue symbols represent the various surface weather stations. The magenta star represents the approximate locations of the two initial fire ignitions, which are ∼550 m apart.

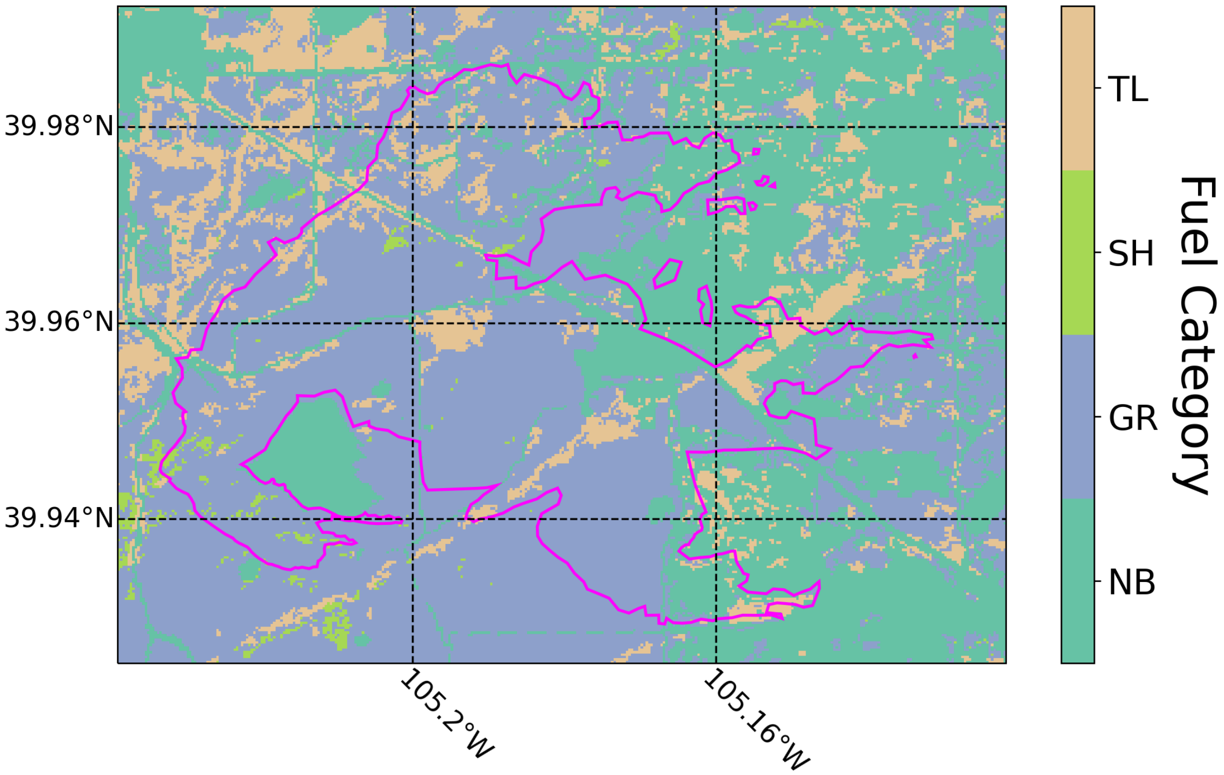

Figure S2. The Anderson 13 fuel model layers used in the WRF-Fire simulation. The final observed fire perimeter is shown in magenta. Fuel categories represent the fuel type of the fuel model;timber litter (TL), shrub (SH), grass (GR), and nonburnable (NB). Note that the slash-blowdown category is not shown due to the absence of this fuel type in our domain.

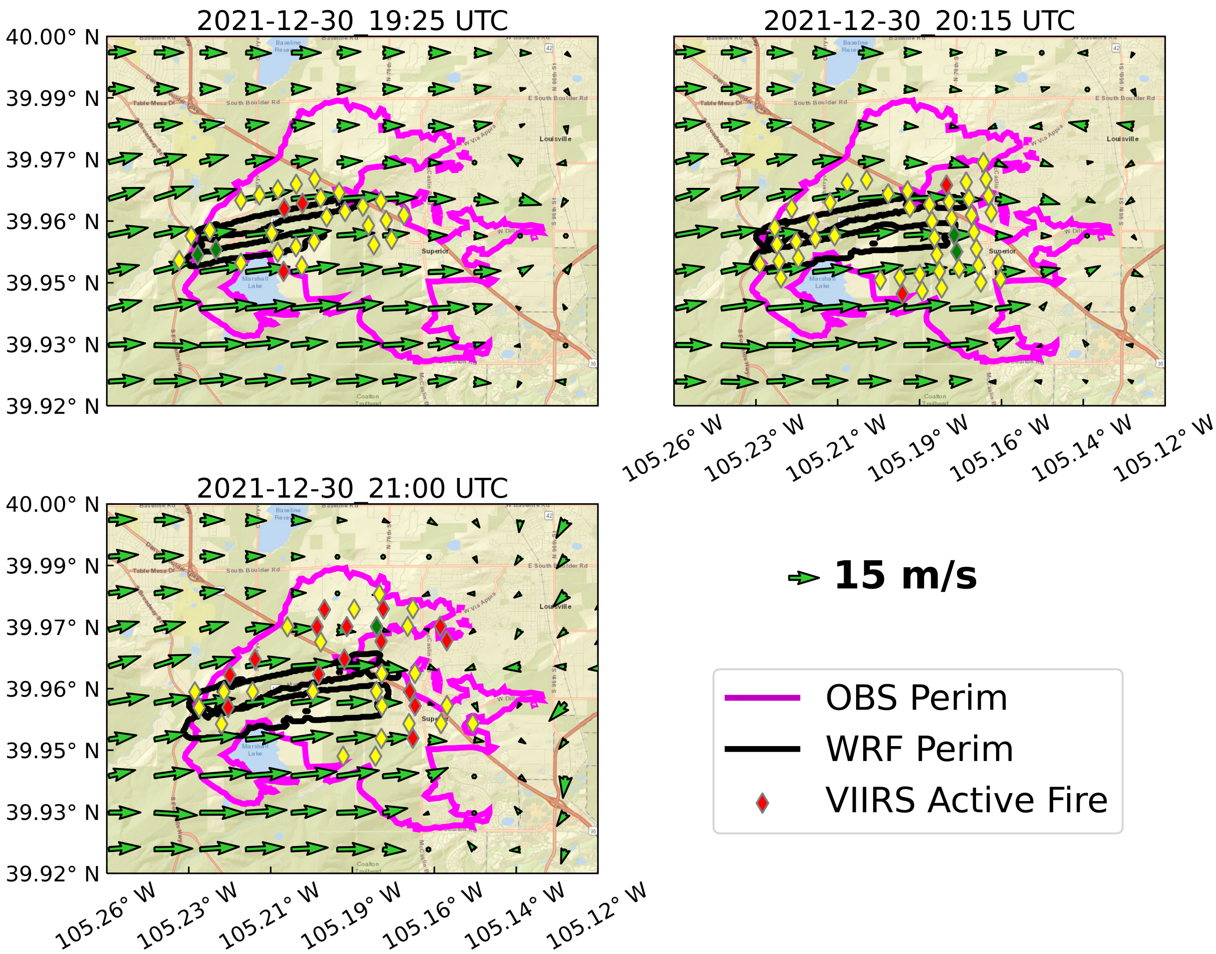

Figure S3. Temporal progression of the Marshall Fire spread. The magenta line represents the final observed perimeter and the black line represents the WRF-Fire perimeter at the indicated time. The colored diamonds represent VIIRS fire detections, with red, yellow, and green representing low, nominal, and high confidence intervals, respectively. Also shown are 10 m wind arrows with wind speed according to the key.

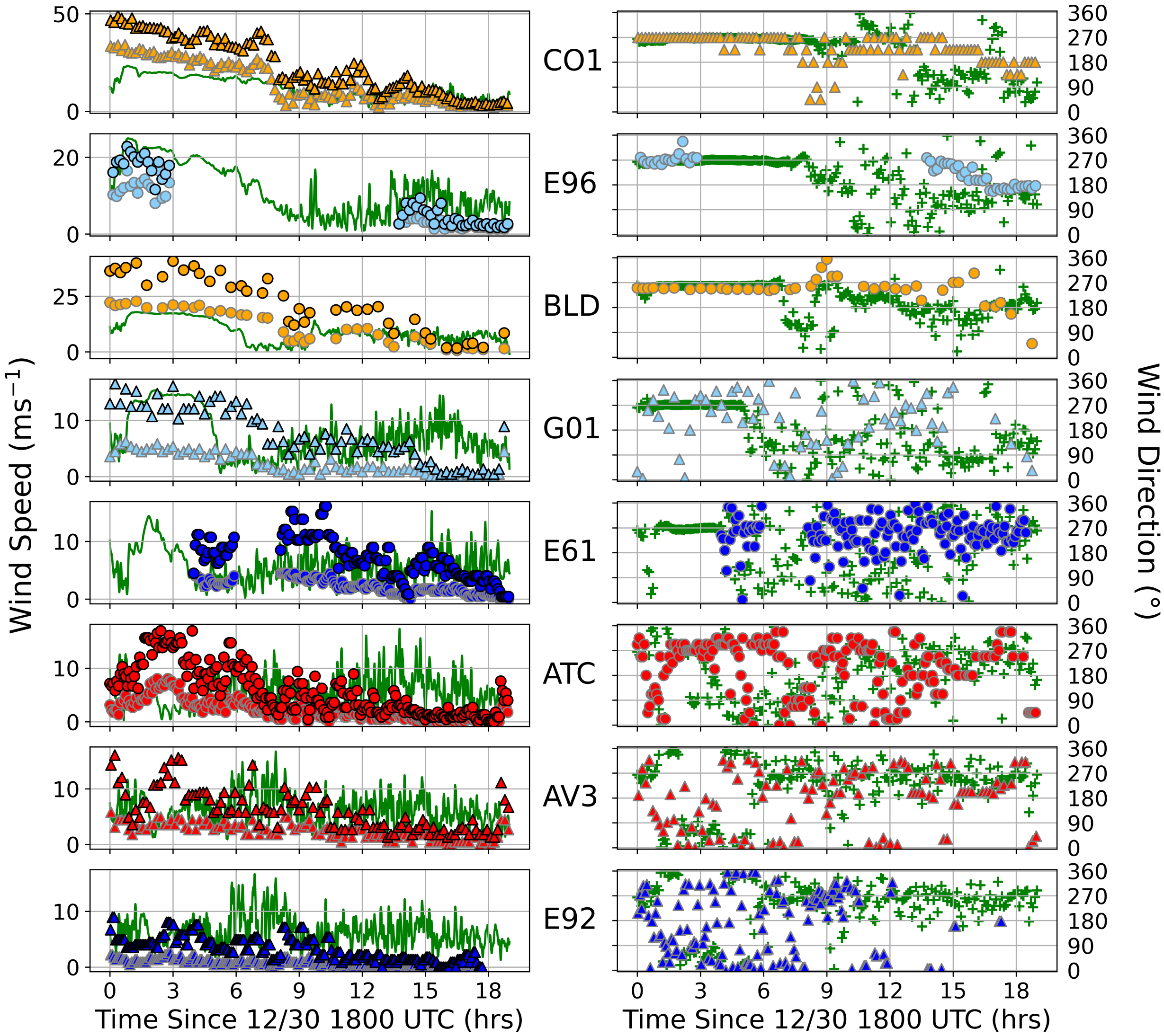

Figure S4. Time series of (left panels) wind speed and (right panels) wind direction for the various surface weather station locations. Green lines represent high-frequency ($\frac{2}{3}$ s) output from WRF, while the symbols represent observations. For the left panels, the light and dark colored symbols show the observed wind speeds and gusts, respectively.

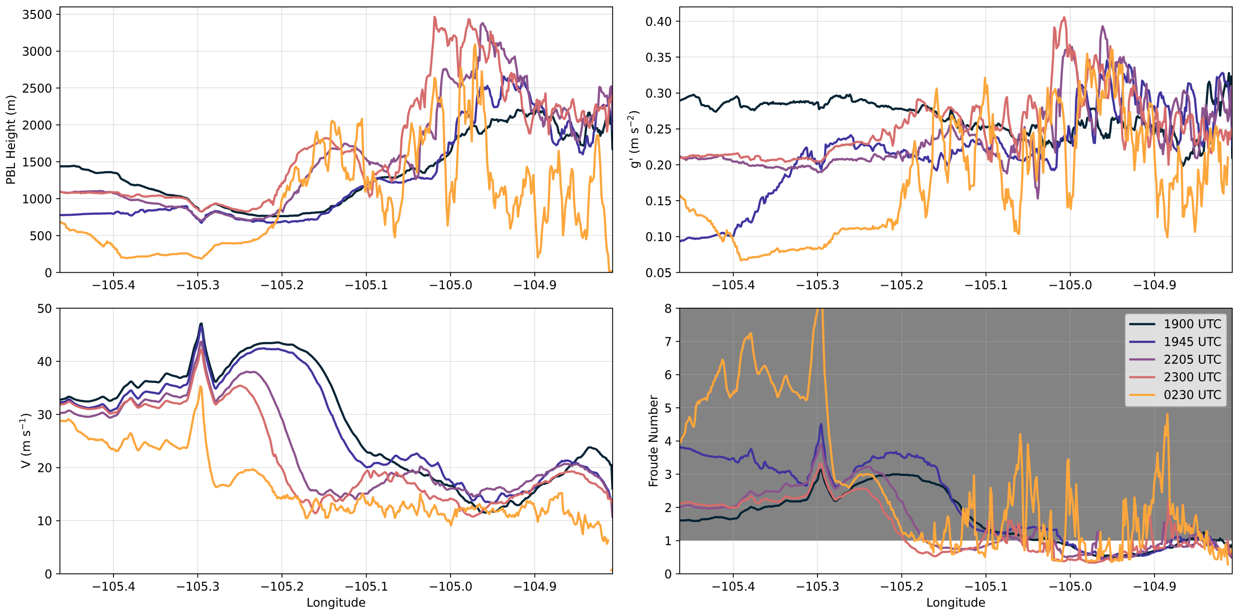

Figure S5. Fr analysis along the east-west transects in Fig. 4 showing: (top left) PBL height, (top right) reduced gravity, g$'$, (bottom left) mean PBL wind speed, and (bottom right) Fr. The shaded region in the bottom right panel represents the supercritical flow region (Fr >1). Details about the Fr calculation are outlined in Text S3.

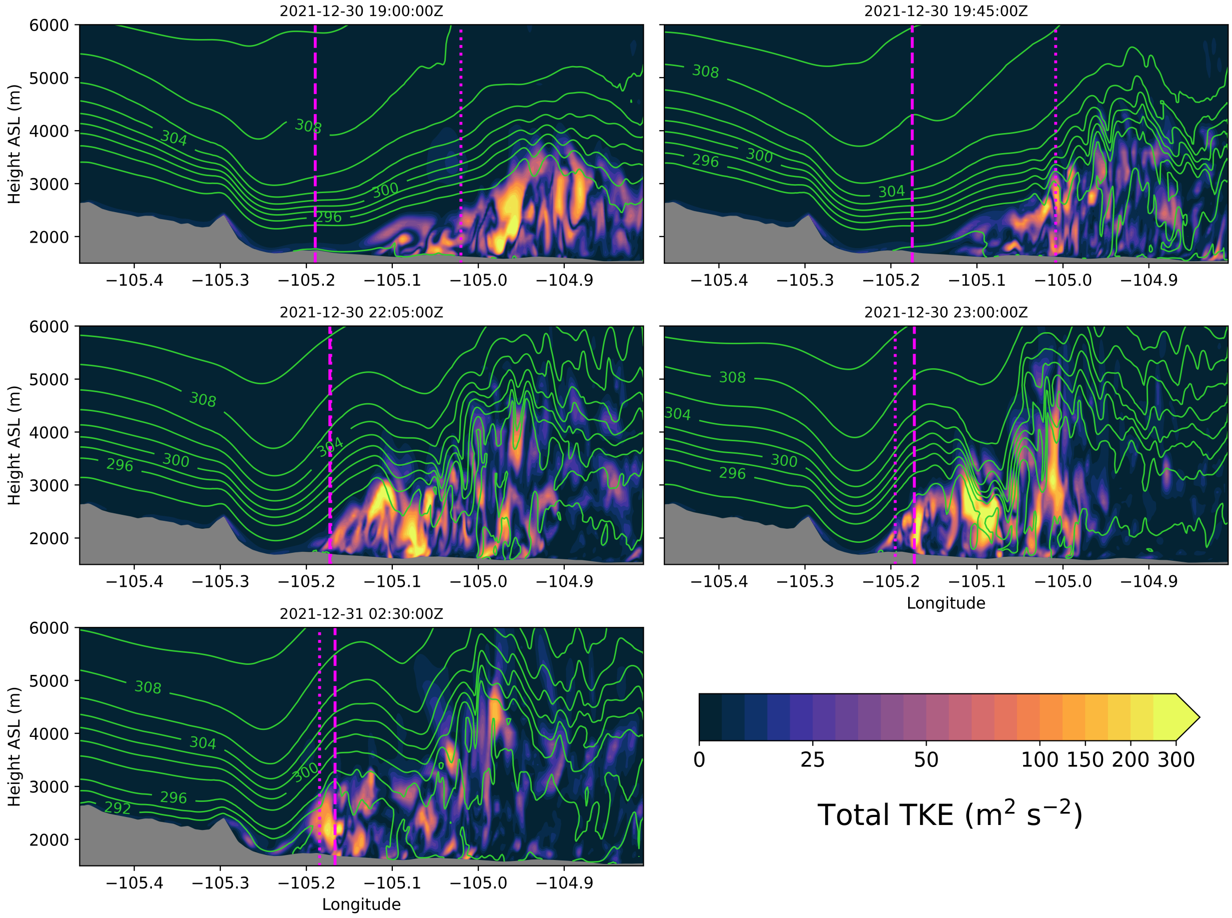

Figure S6. As in Fig. 4, except showing total (resolved plus SGS) TKE according to the colorbar. Also plotted is the location of the flow transition (Fr =1; dotted magenta line) tr Details about the TKE calculation are outlined in Text S4.

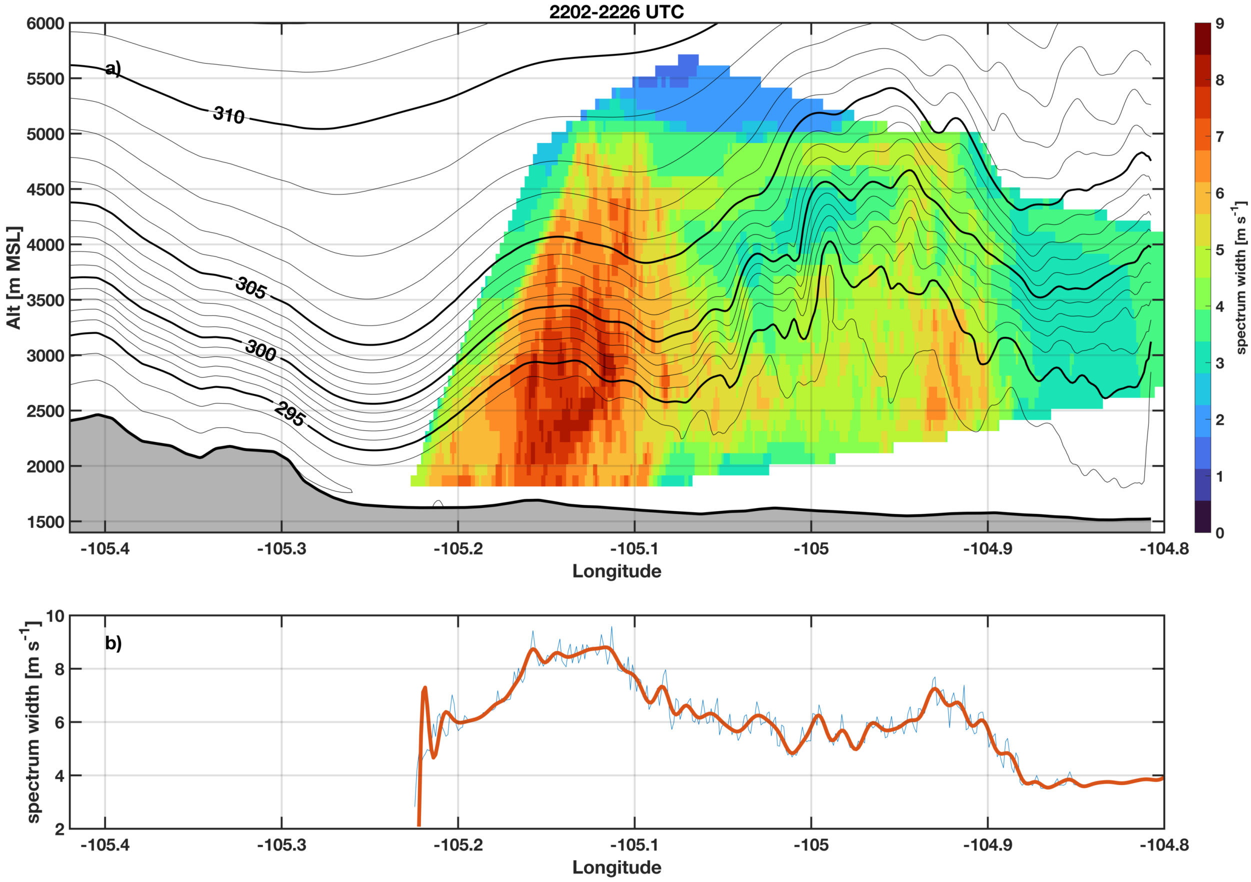

Figure S7. As in Fig. 5, except showing spectrum width.